JGR Atmospheres

RESEARCH ARTICLE
10.1029/2025JD043960

Diurnal Cycle of Extreme Rainfall Over the Dabie Mountain in Summer Under Typical Synoptic Patterns and Associated Mechanisms

Churui Chen[1,2,3], Kun Zhao[1,2,3], Anning Huang[2,3], Ang Zhou[1,2,3], Chenli Wang[2,3], Yinghui Lu[1,2,3], and Shuguang Wang[1,2,3]

[1]State Key Laboratory of Severe Weather Meteorological Science and Technology, Nanjing University, Nanjing, China, [2]Key Laboratory of Mesoscale Severe Weather/MOE and School of Atmosphere Sciences, Nanjing University, Nanjing, China, [3]China Meteorological Administration Radar Meteorology Key Laboratory, Nanjing, China

Key Points:

- Summer extreme rainfall in the Dabie Mountain is most likely to occur under strong southwesterly monsoon
- The Dabie Mountain effectively locks the center of extreme rainfall on the southwestern windward slope
- Diverse interactions among the large-scale circulations, weather systems, and terrain contribute to different diurnal cycles of extreme rainfall

Correspondence to:

K. Zhao,
zhaokun@nju.edu.cn

Citation:

Chen, C., Zhao, K., Huang, A., Zhou, A., Wang, C., Lu, Y., & Wang, S. (2025). Diurnal cycle of extreme rainfall over the Dabie Mountain in summer under typical synoptic patterns and associated mechanisms. *Journal of Geophysical Research: Atmospheres*, *130*, e2025JD043960. https://doi.org/10.1029/2025JD043960

Received 25 MAR 2025
Accepted 4 AUG 2025

Abstract Summer extreme rainfall frequently occurs in the Dabie Mountain (DM). The combined effects of synoptic patterns and local topography on the spatiotemporal variations of extreme rainfall in the summers from 2008 to 2020 have been investigated using an objective classification method. Results show that extreme rainfall in the DM mainly occurs under two typical synoptic patterns (P1 and P2). In the lower troposphere, the P1 type is characterized by southwesterly (easterly) winds south (north) to the DM, while the P2 type features southwesterly winds over the DM. These differences arise from the varying position of the Meiyu front. Under both types, extreme rainfall intensity reaches its diurnal maximum at around 09:00 local solar time (LST) because the low-level southwesterly ageostrophic wind peaks in the early morning induced by inertial oscillation. The southwesterly ageostrophic winds bring abundant water vapor into the DM, resulting in the extreme rainfall along the windward slope. Extreme rainfall intensity decreases rapidly after 09:00 LST under the P2 type but sustains its maximum level for several hours under the P1 type. Two factors contribute to the prolonged high extreme rainfall intensity under the P1 type. One is the convergence between southwesterly and northeasterly ageostrophic flows over the DM. The other is the strengthening of the low-level vortice over the DM from late morning to early afternoon. Overall, the synoptic patterns influence extreme rainfall by regulating the low-level ageostrophic winds and the interactions between multi-scale systems and the DM.

Plain Language Summary Summer extreme rainfall often occurs in the DM. This study explores how the interactions between atmospheric circulations and local terrain influence the daily timing and geographic distribution of extreme rainfall in the summers from 2008 to 2020. The results show that extreme rainfall is most common under two typical circulation patterns (Pattern 1 and Pattern 2). Under Pattern 1, winds blow from the southwest south of the DM and the east north of the DM. Under Pattern 2, southwesterly winds dominate over the DM. Under both patterns, extreme rain peaks around 09:00 AM along the windward slopes, since the humid southwesterly ageostrophic winds peak in the early morning. After 09:00 AM, the rain decreases quickly under Pattern 2 but keeps at the maximum level for several hours before decreasing under Pattern 1. Two factors contribute to the longer high extreme rainfall intensity under pattern 1. First, upward motion increases when northeasterly ageostrophic winds north of the DM meet the southwesterly ageostrophic winds south of it. Second, a weather disturbance develops over the DM, strengthening from late morning into early afternoon. Overall, synoptic patterns shape when and where extreme rainfall occurs by controlling low-level ageostrophic winds and how different weather systems interact with the DM.

1. Introduction

The Yangtze-Huai River Basin (YHRB) suffers from extreme rainfall every summer (from June to August), resulting in severe floods and significant economic losses in this region. The main extreme rainfall episode of the YHRB in the summer is called Meiyu, normally starting in early June and ending in mid July. It is caused by an east-west-oriented elongated rainband associated with a quasi-stationary front (Ding, 1992; Tao, 1987). Along the frontal zone, mesoscale convective systems (MCS) have been observed to form and develop under favorable conditions, directly leading to most of the local extreme rainfall events (Ding, 1993; Fang, 1985; Ninomiya, 2000). The terrain of the YHRB is generally flat but complexly distributed with isolated mesoscale mountains (Zheng et al., 2016). The Dabie Mountain (DM) (as shown in Figure 1), with its main peaks exceeding 1,500 m (Wang & Tan, 2006), is one of the most representative and relatively isolated mesoscale

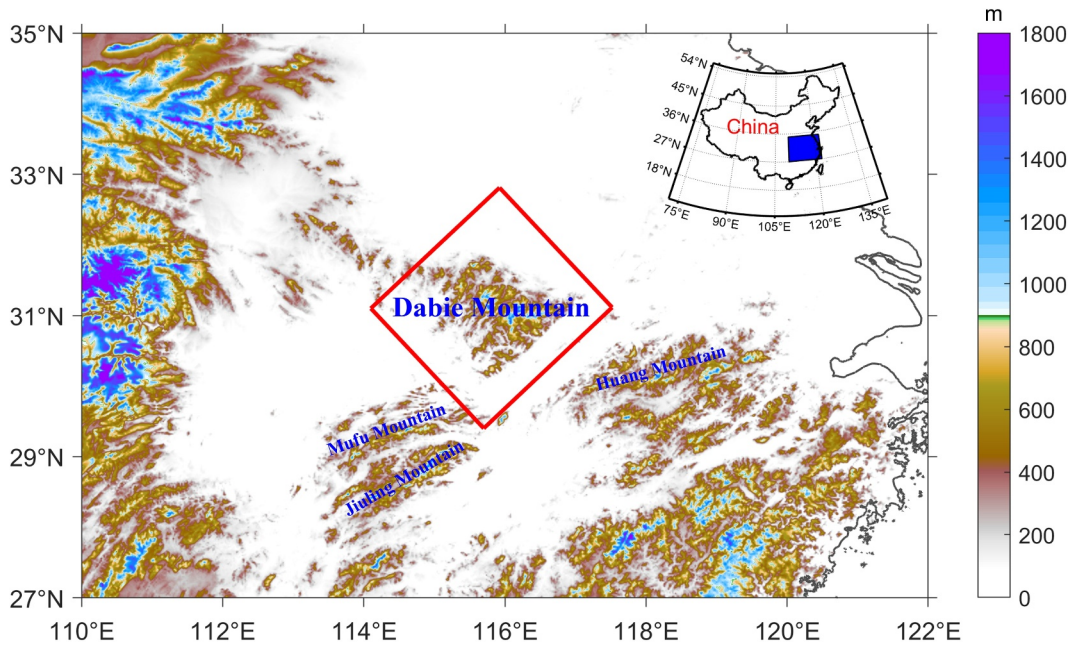

Figure 1. Terrain height distribution of the YHRB. The DM region is marked by the red rectangle. The area used for the PCT is represented by the blue rectangle in the small map. The range of the large figure is also the area used for the PCT.

mountains in the YHRB. Located in the background of several multi-scale weather systems, the DM is identified as one of the topographic rainfall centers of the YHRB in summer (Ni et al., 2018; Wu et al., 2022; F. Zhang et al., 2020; A. Zhang et al., 2020; Zhang & Wang, 2021). It also plays an important role in the initiation, development, and propagation of mesoscale convection along the Meiyu rainband (Sun et al., 2004; Wang et al., 2016; Wang & Tan, 2009; Zheng et al., 2020). Therefore, investigating the features of extreme rainfall in the DM is of great importance in recognizing and understanding the underlying mechanism of extreme rainfall more thoroughly and further reducing losses caused by hazards (Carbone et al., 2002).

The diurnal variation of precipitation, as feedback from certain thermal and dynamical drivers resulting from different environmental conditions and inhomogeneous underlying surfaces, exhibits distinct regional and seasonal characteristics (Dai, 2001; Wallace, 1975; Yang & Slingo, 2001; Yu et al., 2014; Yuan et al., 2012). In the YHRB, the diurnal cycle of Meiyu precipitation has a bimodal structure in atypical Meiyu years but only one peak at 09:30 LST during normal Meiyu years (F. Zhang et al., 2020; A. Zhang et al., 2020). Zeng et al. (2023) also suggest that the diurnal cycle of Meiyu precipitation shows one predominant morning (or late afternoon) peak when the Meiyu front is strong and located relatively southward (or weak and located northward).

In addition to the characteristics of the diurnal variation of summer precipitation, previous studies have also revealed the possible underlying mechanisms. The afternoon peak is generally associated with convective precipitation. This type of precipitation results from the thermal instability caused by solar heating during the daytime so it occurs frequently in the afternoon (Xu & Zipser, 2011). However, the morning precipitation peak in the YHRB is driven by complex factors, with three mechanisms proposed so far to explain it. The first mechanism is the establishment of a low-level jet with abundant moist air in the early morning. The boundary-layer jet at the height of 1,200 m over the YHRB is established in the early morning due to the inertial oscillation of low-level wind fields (Fu et al., 2019; Xue et al., 2018). It exhibits a clear occurrence peak three to 4 hours before the rainfall peak (Cui et al., 2023; Du et al., 2012). The second mechanism involves multiscale thermal circulations induced by the topographic forcing. The large-scale mountain-plain solenoid (MPS) between the central mountains and the eastern plains has a distinct upward branch from nighttime to early morning over the plains, which strengthens the morning rainfall (Chen et al., 2012; Sun & Zhang, 2012; Zhang et al., 2014). The land-sea breezes (Chen et al., 2014; Wang et al., 2021) and the localized MPS (He & Zhang, 2010) also contribute to the morning precipitation peak. The third mechanism is associated with the life cycle of the mesoscale convective vortices (MCVs). There are two types of MCVs associated with the diurnal cycle of extreme rainfall near the DM, both of

which are meso-α-scale convective systems with a horizontal scale of approximately 300 km (Ding, 1992; Fang, 1985). One is the MCVs defined as the Dabie vortices (DBVs), which are triggered most frequently at 06:00 LST and 18:00 LST near the DM (Fu et al., 2017; Zhang et al., 2015). The other is the eastward-propagating MCVs along the Meiyu rainband, which normally arrive at the DM and adjacent areas from morning to late afternoon, bringing rainfall to the regions they pass through (Zhang et al., 2018).

As mentioned above, previous research has mainly focused on the diurnal variations and the underlying mechanisms of large-scale precipitation, such as precipitation in the YHRB and South China. However, there is a lack of a systematic explanation for the mechanisms of the diurnal variations of localized precipitation, such as mesoscale orographic precipitation. Moreover, numerical simulation and case studies have frequently been used to investigate the physics of the diurnal cycles of precipitation under specific circulation backgrounds. The understanding of the long-term statistical characteristics and mechanisms of precipitation under different synoptic patterns remains quite limited. Therefore, this study aims to address the questions as follows: What are the typical synoptic patterns dominating the extreme rainfall in the DM? What are the characteristics of the spatial distribution and diurnal cycles of extreme rainfall under different synoptic patterns? What are the underlying mechanisms of the diurnal cycles of extreme rainfall under different synoptic patterns?

The rest of the paper is organized as follows: Section 2 describes the data and methods used in this research. The spatiotemporal distribution of extreme rainfall under typical synoptic patterns and the possible mechanisms responsible for the diurnal variations of extreme rainfall are presented in Section 3 and Section 4 respectively. Section 5 provides the summary and discussion.

2. Data and Methods

2.1. Observational and Reanalysis Data

The high spatiotemporal precipitation product for the summers (June–August) from 2008 to 2020 is provided by the National Meteorological Information Center of China (Shen et al., 2014). This product is generated based on rain gauge observations and the CMORPH (The Climate Prediction Center morphing method) precipitation product (Joyce et al., 2004) over China using probability density function-optimal interpolation (PDF-OI) methods (Shen et al., 2014). This data set with hourly temporal resolution and $0.1° \times 0.1°$ horizontal resolution can capture detailed information on rainfall in the DM.

The fifth generation of the ECMWF (European Center for Medium-Range Weather Forecasts) atmospheric reanalysis (ERA5) data set in the summers from 2008 to 2020 is used to classify the synoptic patterns and investigate the environmental characteristics of extreme rainfall. This data set with a horizontal resolution of 0.25° and temporal resolution of 1 hr has 37 vertical levels ranging from 1,000 to 1 hPa in total, providing precise estimation of historical atmospheric quantities consistently (Hersbach et al., 2020). Previous studies have used ERA5 data to classify large-scale circulations in the YHRB, providing a basis for using the data set in the present study (Clark et al., 2021; Xu et al., 2023; Zeng et al., 2023; Zhang et al., 2021).

2.2. Criteria for Identifying the Extreme Rainfall Days

Based on the hourly precipitation data during the summers from 2008 to 2020, the daily accumulated precipitation (PA) is first computed as the regionally averaged total precipitation for each day in the DM region. A day is classified as a rainfall day if the daily mean precipitation (PI), defined as PA divided by 24 hr, exceeds 0.1 mm/hr. The peaks-over-threshold method (Jones et al., 1999) is used to identify the extreme rainfall days for which PA is considered extreme to the rest of the rainfall days. Compared to fixed definitions of extreme precipitation, this percentile-based method can be applied across diverse regions and time periods regardless of seasonal and regional variations, and has been widely adopted in previous studies (Tu et al., 2010; Yan et al., 2019). In the present study, the threshold is set at the 90% percentile, and the DM region is denoted by the red rectangle in Figure 1 (Wang et al., 2021). There are 1,094 rainfall days in total, among which 109 are classified as extreme rainfall days. These extreme rainfall days have PA exceeding 19.89 mm/day and contribute to approximately 60% of the total cumulative PA in the DM during summer (Figure 2b).

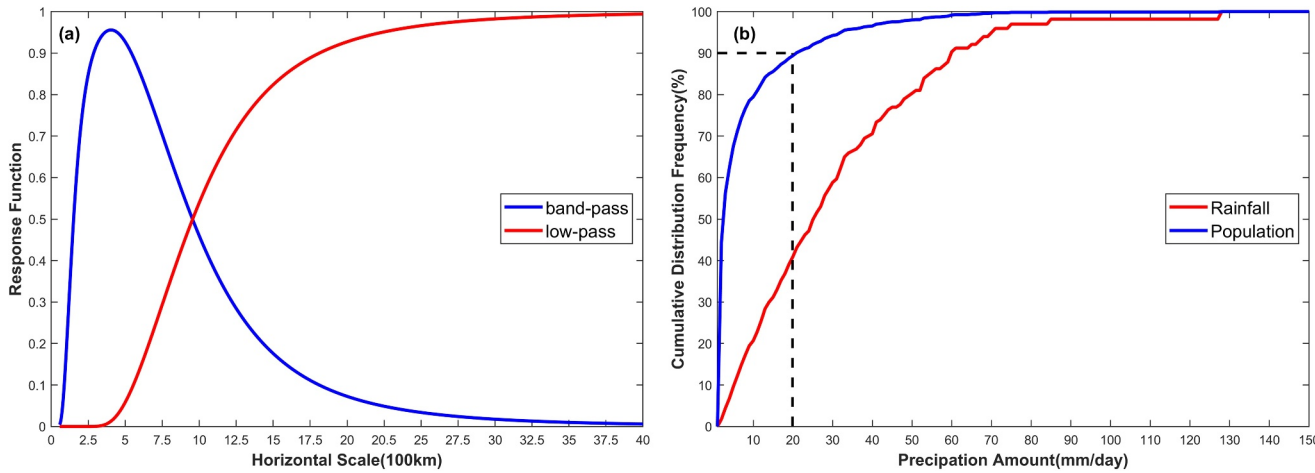

Figure 2. (a) Response function of the mesoscale band-pass filter (red) and the low-pass filter (blue) in terms of wavelength following Barnes (1973). (b) Cumulative percentage (blue line) and cumulative PA percentage (red line) of rainfall days whose PA is below a certain number. The black dashed lines indicate that the PA of the top 10% rainfall days is above 19.89 mm/day.

2.3. Objective Synoptic Classification Method

The obliquely rotated principal component analysis in *T* mode (PCT hereafter) is applied to the ERA5 reanalysis data to objectively classify synoptic-scale circulations over the YHRB (Huth, 1993, 1996a, 1996b, 2000). PCT is based on rotational principal component analysis (PCA) but arranges the input matrix differently, with the columns representing the observing time and the rows representing the grid points. This method has been integrated into an open-source software package called "cost733class" (Philipp et al., 2010, 2016).

Studies have been conducted to investigate the circulation patterns over China based on the PCT method (He et al., 2017; Rao et al., 2019; Wang et al., 2021; Xu et al., 2022). There are several reasons why PCT is chosen among many circulation classification methods in the present work. On one hand, several experiments have been conducted on the same data set to compare the effects of k-means, SOM (self-organizing map), and PCT based on the cost733class algorithm. Results show that the three methods yield similar circulation patterns. On the other hand, several studies have demonstrated that PCT is highly effective at reflecting the underlying physical mechanisms and is less dependent on the choice of pre-set parameters compared to other classification methods (Huth, 1996a, 1996b; Philipp, 2009). Given that one of the aims of this study is to explore the underlying physical mechanisms of circulations, PCT is a relatively more suitable method.

2.4. Barnes Band-Pass Filter

The analysis of mesoscale systems needs to be based on high-spatiotemporal resolution observations. However, it is difficult to obtain long-term historical observation data (Chen, 1994). The Barnes band-pass filter is an objective time-to-space analysis technique (Barnes, 1973) that can be used to extract mesoscale information from conventional data. A band-pass filter can be obtained by the difference between two low-pass filters (Xu & Ding, 1988). Details including equations and some pre-set parameters can be found in Appendix A of Xu et al. (2017).

In the present study, the Barnes filter is used in two ways. First, the horizontal wind (U and V hereafter) and the relative vorticity (RV hereafter) at 875 hPa are filtered using two low-pass filters. The components U_1, V_1, and RV_1 are obtained by passing the U, V, and RV through the first low-pass filter with $g = 0.3$ and $c = 1{,}500$. The components U_2, V_2, and RV_2 are obtained by passing the U, V, and RV through the second low-pass filter with $g = 0.3$ and $c = 60{,}000$. The mesoscale components U_m, V_m, and RV_m are then computed by subtracting U_1, V_1, and RV_1 from U_2, V_2, and RV_2. The response function for the mesoscale band-pass filter is plotted by the blue line in Figure 2a. The plot indicates that waves between 200 and 1,000 km are mostly retained, comparable to the horizontal scale of the MCV. Second, the geopotential height at 875 hPa is filtered using a low-pass filter by choosing $g = 0.3$ and $c = 30{,}000$ to get the geostrophic wind field following Xue et al. (2018). The response function for the low-pass filter is plotted as the red line in Figure 2a. The low-pass filter applied to the geopotential

height damps out waves shorter than 500 km while allowing waves longer than 1,000 km to pass, thereby minimizing noise in the geostrophic winds calculated from the geopotential height.

2.5. Calculation of the Momentum Budget Analysis

Analysis of the momentum budget is conducted to investigate the mechanisms responsible for the diurnal variation in wind field. Following Du et al. (2015) and Fu et al. (2019), the horizontal momentum equation can be written as Equations 1 and 2:

$$\underbrace{\frac{\partial u}{\partial t}}_{1} = \underbrace{-\left(u\frac{\partial u}{\partial x}+v\frac{\partial u}{\partial y}\right)}_{2}\underbrace{-\omega\frac{\partial u}{\partial p}}_{3}\underbrace{-\frac{\partial \varphi}{\partial x}}_{4}\underbrace{+fv}_{5}\underbrace{+F_{rx}}_{6}; \tag{1}$$

$$\underbrace{\frac{\partial v}{\partial t}}_{1} = \underbrace{-\left(u\frac{\partial v}{\partial x}+v\frac{\partial v}{\partial y}\right)}_{2}\underbrace{-\omega\frac{\partial v}{\partial p}}_{3}\underbrace{-\frac{\partial \varphi}{\partial y}}_{4}\underbrace{-fu}_{5}\underbrace{+F_{ry}}_{6}; \tag{2}$$

The six terms of Equations 1 and 2 represent the tendency of wind (TW, term 1), horizontal advection (HA, term 2), vertical advection (VA, term 3), pressure gradient force (PGF, term 4), Coriolis force (CF, term 5) and frictional force (FF, term 6). Since there is no explicit method for calculating FF, term 6 is determined by subtracting the sum of terms 2 through 5 from term 1. The advection term (AD) is the sum of terms 2 and 3. The Coriolis force on the ageostrophic wind term (CFA) is calculated by adding terms 4 and 5 which can be explained by Equations 3 and 4 as follows (Luo & Du, 2023):

$$PGF = -\nabla\varphi = f\vec{k}\times\vec{v_g}; \tag{3}$$

$$PGF_y + CF_y = -\frac{\partial \varphi}{\partial y} - fu = fu_g - fu = -fu_a = CFA_y; \tag{4}$$

In order to further clarify the causes of the diurnal variation in ageostrophic wind, the diagnostic equations of ageostrophic wind are derived from the horizontal momentum equations following Xia et al. (2023):

$$u_a = \underbrace{-\frac{1}{f}\frac{\partial v}{\partial t}}_{1}\underbrace{-\frac{1}{f}\left(u\frac{\partial v}{\partial x}+v\frac{\partial v}{\partial y}\right)}_{2}\underbrace{+\frac{R\omega}{pf^2}\frac{\partial T}{\partial x}}_{3}\underbrace{-\frac{\omega}{f}\frac{\partial v_a}{\partial p}}_{4}\underbrace{+\frac{1}{f}F_{rv}}_{5}; \tag{5}$$

$$v_a = \underbrace{\frac{1}{f}\frac{\partial u}{\partial t}}_{1}\underbrace{+\frac{1}{f}\left(u\frac{\partial u}{\partial x}+v\frac{\partial u}{\partial y}\right)}_{2}\underbrace{+\frac{R\omega}{pf^2}\frac{\partial T}{\partial y}}_{3}\underbrace{+\frac{\omega}{f}\frac{\partial u_a}{\partial p}}_{4}\underbrace{-\frac{1}{f}F_{ru}}_{5}; \tag{6}$$

The five terms on the right-hand side of Equations 5 and 6 represent the following: the local wind tendency (LT, term 1), inertial advection (IA, term 2), baroclinic effects due to the temperature gradient (BE, term 3), vertical transport of the ageostrophic wind (VTA, term 4), and boundary layer friction (BLF, term 5). Term 5 is calculated by subtracting the sum of terms 1 through 4 from the total ageostrophic wind. Since the VTA term is significantly smaller than the other four terms, it is not analyzed in the present study.

3. Spatiotemporal Distribution of Extreme Rainfall Under Typical Synoptic Patterns

3.1. Characteristics of Synoptic Patterns and Distribution of Associated Extreme Rainfall

In the present study, PCT is applied to the standardized ERA5 geopotential height, horizontal wind, and temperature at different levels (200, 700, and 850 hPa) over the YHRB (110°E–122°E, 27°N–45°N) during rainfall days in the summers from 2008 to 2020 (1,094 days in total) to get four synoptic patterns. The levels, variables, and domain size used for the classification are chosen based on several experiments to obtain the most realistic and physically interpretable circulation patterns. The number of synoptic patterns is determined through a two-step process combining statistical analysis and empirical validation. An elbow point is first identified near the

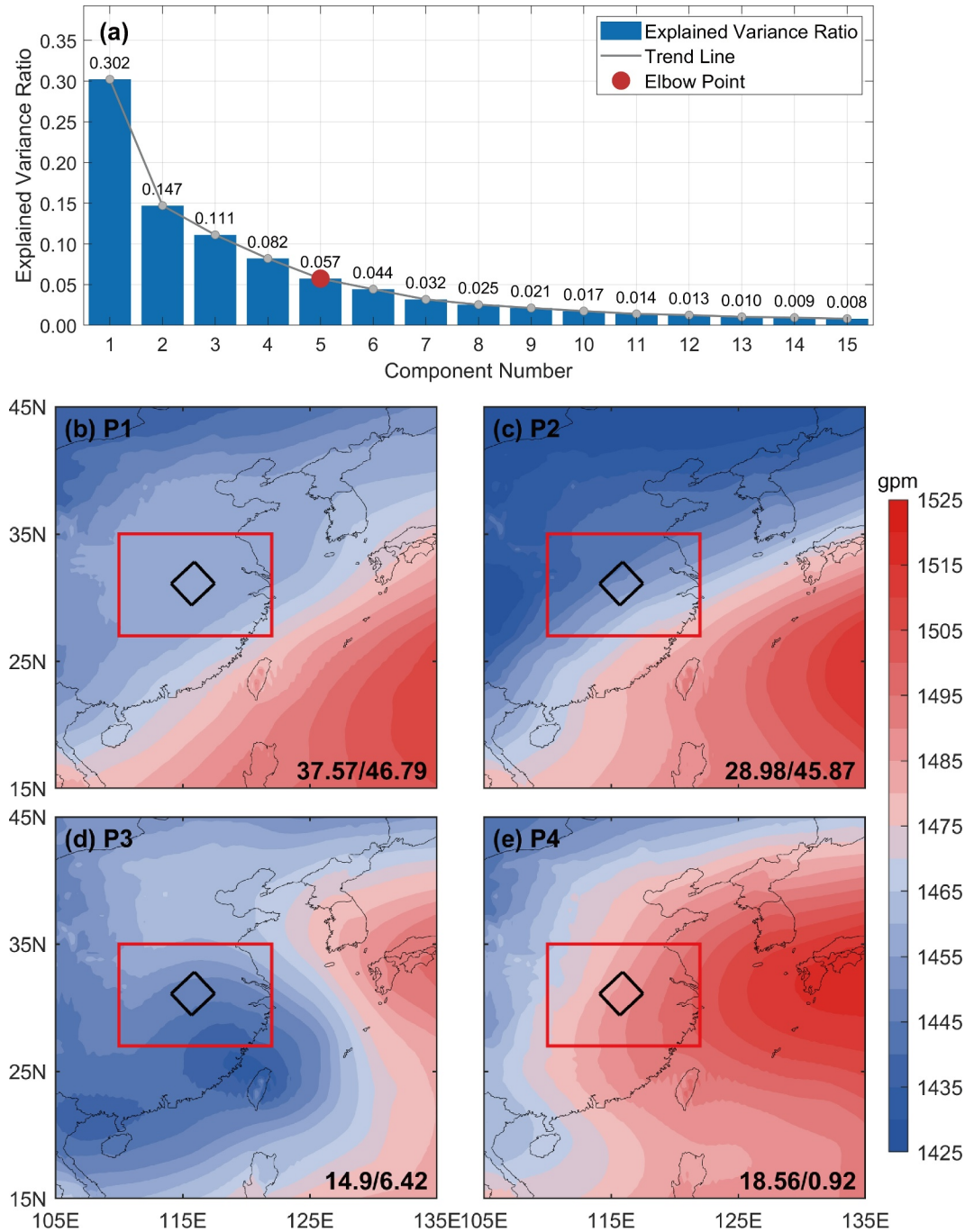

Figure 3. (a) Explained variance ratio of the first 15 principal components before rotation. The blue bars and the black numbers above the bars represent the explained variance ratio of each component, with the gray line and markers showing the decreasing trend. (b–e) The composite mean geopotential height at 850 hPa (shading) under the four synoptic patterns. The first (second) number is the occurrence frequency (unit: %) of each pattern among all rainfall days (extreme rainfall days). The black box indicates the DM and the red rectangle indicates the domain used for the PCT objective synoptic classification.

fifth principal component based on the explained variance curve as indicated in Figure 3a (Cattell, 1966; O'Lenic & Livezey, 1988). However, due to the gradual decline and absence of a clear-cut elbow point, we also conduct PCT on four, five, and six nodes as part of sensitivity testing. Results show that by choosing four nodes, the synoptic patterns are representative and exhibit a low repetition rate.

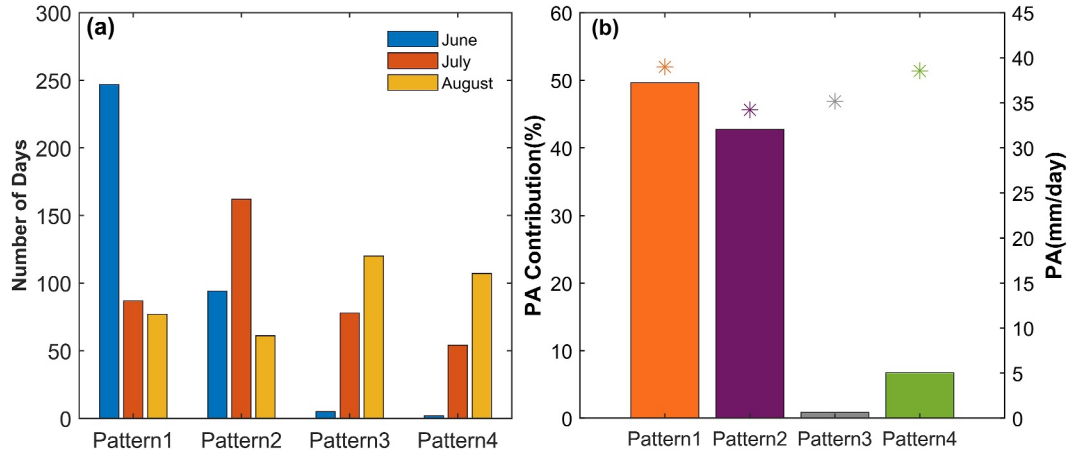

Figure 4. (a) The number of days during different months under each pattern. (b) The contribution of the total extreme rainfall amount under each pattern to the total extreme rainfall amount (bars) and the extreme rainfall amount under each pattern (asteroids).

All four patterns are ranked in descending order of occurrence frequency during the extreme rainfall days in the summers from 2008 to 2020 and their geopotential height at 850 hPa is shown in Figures 3b–3e (hereafter named P1 to P4). The total occurrence of the P1 and P2 types accounts for about 92.66% of the 109 extreme rainfall days and 67.41% of the 1,094 rainfall days (Figures 3b–3e), indicating that extreme rainfall is most likely to occur under these two patterns. Meanwhile, the extreme rainfall amount under the P1 and P2 types constitutes approximately 90% of the total extreme rainfall amount (Figure 4b). Therefore, we treat the P1 and P2 types as the typical synoptic patterns leading to occurrences of extreme rainfall, and they will be analyzed in detail in the rest of the article.

Under the P1 type, the southwesterly (easterly) winds prevail over the southern (northern) side of the DM (Figures 3b and 6a). In contrast, the P2 type is characterized by uniform southwesterly winds over the DM (Figures 3c and 6c). This difference is associated with the northward shift of the Western North Pacific Subtropical High (WNPSH) under the P2 type. This corresponds to the monthly occurrence frequency of synoptic patterns shown in Figure 4a. The P1 and P2 types primarily occur in June and July, aligning with the Meiyu season in East Asia. The P1 type occurs more frequently in June, while the P2 type is more prevalent in July.

As one of the most representative terrains in the YHRB, the DM is a relatively isolated precipitation center (Chen et al., 2024). Figure 5a indicates that the center of extreme rainfall in the DM is located along the southwestern windward slope with an extreme rainfall amount of around 57.6 mm/day. The extreme rainfall amount is greater

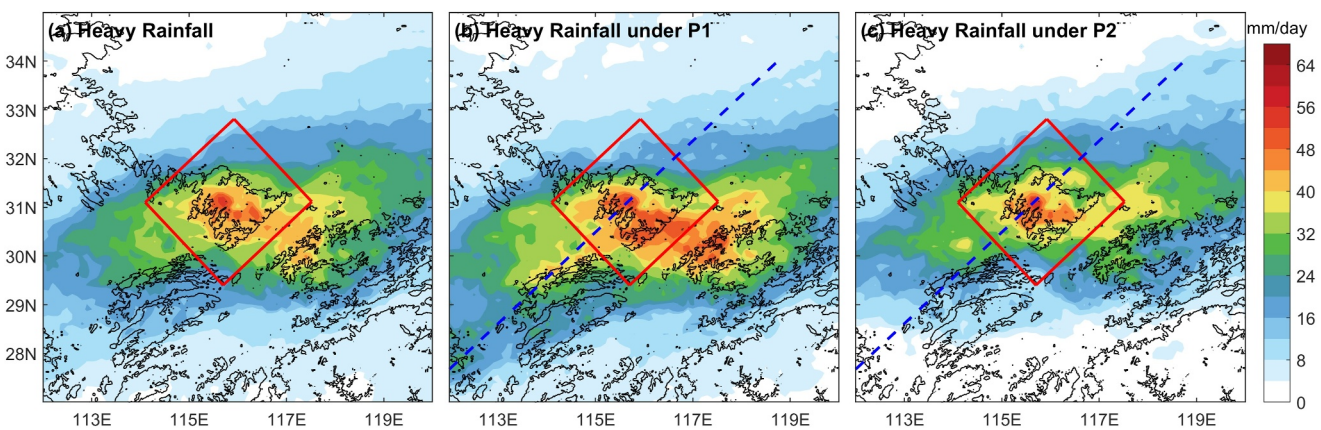

Figure 5. The composite spatial distribution of extreme rainfall amount (shading) and terrain height of 200 and 1,500 m (black lines) on all extreme rainfall days (a), extreme rainfall days under the P1 type (b), and extreme rainfall days under the P2 type (c). The red box is the DM region and the blue dashed line indicates the position of the vertical cross-section.

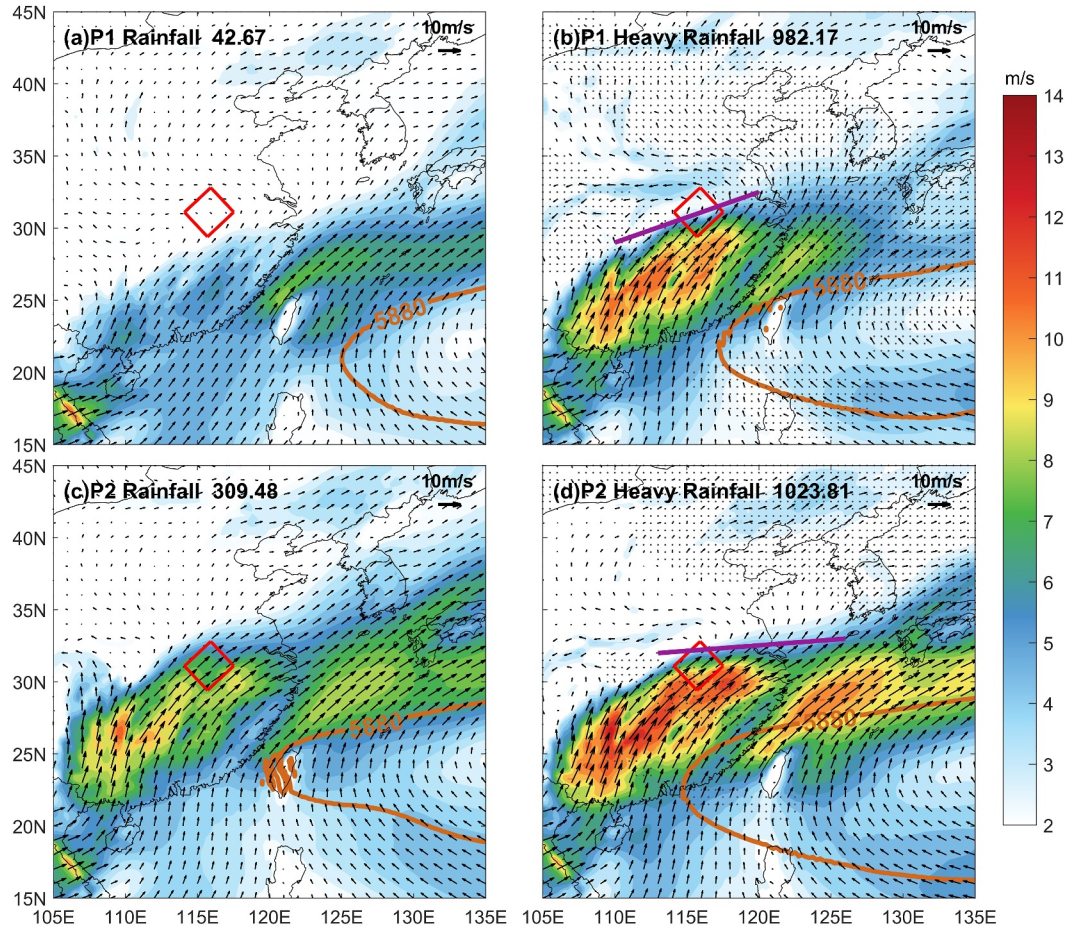

Figure 6. The composite horizontal wind vectors (arrows) and wind speed (shading) at 850 hPa of the P1 type on rainfall days (a) and extreme rainfall days (b). As in panels (c, d), but for the P2 type. The red rectangle is the DM region. The orange solid line is the composite geopotential height of 5,880 at 500 hPa, while the purple solid line in panels (b–d) indicates the position of the front. The region covered by the gray dots in panels (b, d) means that the differences in the geopotential height between the rainfall days and the extreme rainfall days is above the significant level of 0.95. The black numbers in the top left corners of (a–d) represent the net water vapor fluxes entering the DM region.

under the P1 type than under the P2 type (asteroids in Figure 4b), suggesting that both the occurrence frequency and the extreme rainfall amount contribute to the higher total extreme rainfall amount under the P1 type compared to the P2 type. The spatial distribution of extreme rainfall amount under the two typical patterns is presented in Figures 5b and 5c. The strongest extreme rainfall centers are concentrated along the southwestern windward slope under both patterns. We can conclude that the DM plays an important role in locking the extreme rainfall on the windward slope of the terrain effectively. Moreover, a Meiyu front-related, east-west-oriented rainband also develops on the southern side of the mountain under the P1 type, suggesting that the extreme rainfall process under this pattern is more complex.

3.2. Features of Favorable Environments for Extreme Rainfall

The large-scale circulations on extreme rainfall days are similar to those on rainfall days, yet the position and strength differ. Thus, the favorable conditions for extreme rainfall under the P1 and P2 types are investigated in this subsection. The 850 hPa wind field is analyzed because the low-level wind field is directly linked to precipitation and is used for synoptic pattern classification.

The westward extension and intensification of the WNPSH during extreme rainfall days can be observed in the 5,880-gpm contour at 500 hPa in Figure 6, as this contour is commonly used to indicate the position of the WNPSH (Shuqing & Ming, 1999; Zeng et al., 2023). Together with the low-pressure system strengthening to the

west, the increased geopotential height gradient near the DM enhances the southwesterly wind. To further evaluate the relationship between the lower tropospheric environment and extreme rainfall quantitatively, the net moisture fluxes into the DM region through four boundaries are indicated by the black numbers at the top of Figure 6. The moisture flux is vertically integrated from 1,000 to 700 hPa, as it has proven to account for about 80% of the column-integrated moisture flux (Chen et al., 2013, 2017). The prevailing southwesterly winds, carrying abundant warm water vapor from the Bay of Bengal and the South China Sea (Clark et al., 2021; Xue et al., 2018), encounter the DM, causing extreme rainfall along the windward slope.

The Meiyu front also contributes to extreme rainfall under the two patterns. We define the area of a relatively larger meridional gradient of the potential pseudo-equivalent temperature at 850 hPa (larger than 4 K/0.25°) as the general area of the front following Zeng et al. (2023) (purple line in Figures 6b and 6d). Under the P1 type, the front is located over the DM, with the convergence zone of the winds from both sides of the front within the DM region. Under the P2 type, the front shifts northward, pushing the convergence zone beyond the DM region. Thus, the Meiyu front has a greater influence on extreme rainfall under the P1 type than under the P2 type, aligning with the spatial distribution of extreme rainfall shown in Figure 5c.

In summary, during extreme rainfall days, much stronger prevailing southwesterly winds bring sufficient moisture into the DM region under the two synoptic patterns. The humid and warm airflow is blocked and lifted by the terrain leading to the increase of precipitation intensity (Houze, 2012). In addition to the prevailing wind, the interactions between the Meiyu front and the DM are also crucial for the differences of extreme rainfall under different synoptic patterns. In the next section, the diurnal variations of extreme rainfall under the two typical patterns and their underlying mechanisms will be further explored.

4. Possible Mechanisms for the Diurnal Variations of Extreme Rainfall

4.1. Diurnal Cycles of Extreme Rainfall

Figure 7 shows the diurnal variations of the extreme rainfall intensity in the DM region and the spatial distribution of extreme rainfall intensity under the two typical synoptic patterns. The diurnal variations of extreme rainfall under the P1 and P2 types are significantly different from each other.

Under the P1 type, the extreme rainfall intensity increases from midnight to early morning until it reaches 1.94 mm/hr at 06:00 LST. During this time, the precipitation intensifies on the southwestern windward slope of the DM and gradually becomes an extreme rainfall center (Figures 7b and 7c). From 06:00 LST to 08:00 LST, the extreme rainfall center first dissipates, and then the Meiyu front rainbelt in the south part of the DM appears (Figures 7c and 7d). From 08:00 LST to 12:00 LST, the extreme rainfall intensity stabilizes at around 2.1 mm/hr as the Meiyu front rainbelt gradually organizes (Figures 7d and 7e). After 12:00 LST, the extreme rainfall intensity decreases throughout the rest of the day. In general, the extreme rainfall under the P1 type gradually transitions from orographic precipitation to frontal precipitation. Under the P2 type, the extreme rainfall intensity continues to increase in the early morning, reaching its maximum of around 2.21 mm/hr at 09:00 LST and then gradually decreasing. The continuously intensifying precipitation in the morning concentrates on the southwestern windward slope of the DM (Figures 7k–7n); thus the extreme rainfall of the P2 type is primarily manifested as orographic precipitation on the windward slope of the DM.

4.2. Diurnal Cycles of Low-Level Wind

As discussed above, the low-level wind field is closely related to extreme rainfall and its diurnal cycles. In this subsection, the low-level winds are divided into geostrophic and ageostrophic components to further explore the underlying physical mechanisms of the different diurnal cycles of extreme rainfall under the P1 and P2 types. The geopotential height, processed through the Barnes low-pass filter as mentioned in Section 2.3 is used to calculate the geostrophic and ageostrophic winds following equations in Section 2d of Wang et al. (2021).

Under both synoptic patterns, the geostrophic wind speed is about twice that of the ageostrophic wind speed. However, the daily variation in geostrophic wind speed is less than half that of the ageostrophic wind speed, indicating that geostrophic winds remain relatively steady, while ageostrophic winds primarily drive diurnal variations in the wind field (Figure 8). Given that geostrophic winds are non-divergent by definition, convergence and divergence are primarily driven by ageostrophic winds. Therefore, we primarily analyze the diurnal variations in ageostrophic winds and their impacts on the diurnal cycles of extreme rainfall.

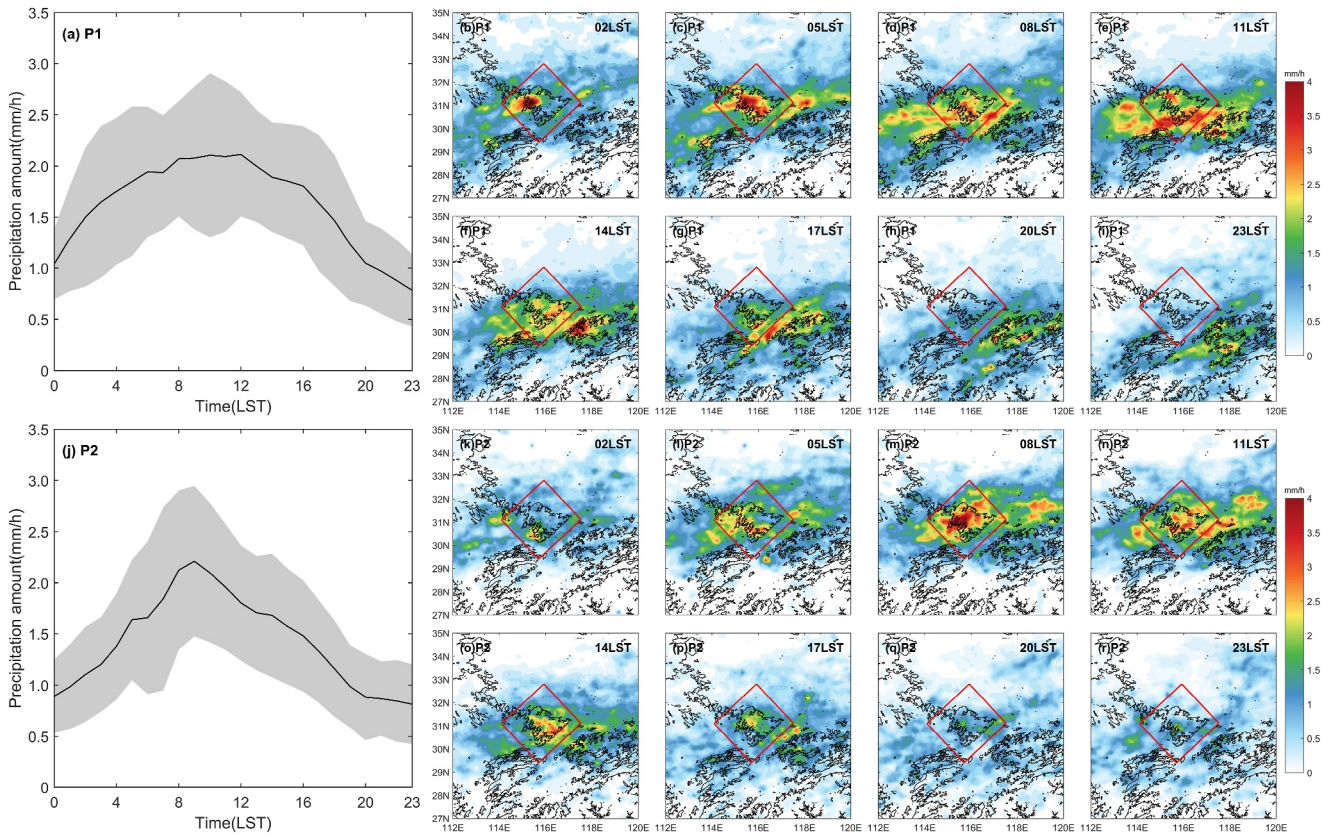

Figure 7. Diurnal variations of regionally-averaged extreme rainfall intensity (black lines, the DM region denoted by the red rectangle) and the range of standard deviation (shading) under the P1 (a) and P2 types (j). The spatial distribution of extreme rainfall intensity every 3 hours starting from 02:00 LST of the P1 type is shown from (b to i). As in (k–r), but for the P2 type. The black solid lines indicate the terrain height of 200 and 1,500 m.

Figures 8a–8e show the diurnal variation in ageostrophic winds on the extreme rainfall days under the P1 type along vertical cross-sections (blue dashed line in Figure 5). The selected vertical cross-section passes through the extreme rainfall center on the southwestern windward slope of the DM and is oriented perpendicular to the slope. Given that the low-level southwesterly winds are also nearly perpendicular to this slope (Figure 6), the cross-section aligns with the low-level southwesterly winds over this region. The horizontal ageostrophic wind of the vertical cross-section consists of the superposition of the u and v components of the ageostrophic wind projected onto the plane.

Under the P1 type, low-level southwesterly geostrophic wind prevails in the southwestern DM, while northeasterly geostrophic wind dominates the northeast. The southwesterly ageostrophic wind over the southern DM peaks around 03:00 LST (Figure 8b), with convergence maximizing two hours later at 950 hPa (0.45×10^{-5} s^{-1}). In the early morning, strong and moist low-level southwesterly ageostrophic wind, superimposed on southwesterly geostrophic flow (Figure 8g), converges upstream of the DM. The DM continuously blocks and lifts the prevailing southwesterly wind throughout the day, with these effects intensifying in the morning as the southwesterly wind peaks. This process ultimately triggered the precipitation peak on the southwestern windward slope several hours later, consistent with Xue et al. (2018). This time lag is primarily attributed to the development of moist convection (Fu et al., 2019). Subsequently, the northeasterly ageostrophic wind on the northeastern side strengthens and peaks at 07:00 LST. At 875 hPa above the DM, it converges with the southwesterly ageostrophic wind along the front, reaching a maximum convergence of 0.4×10^{-5} s^{-1} (Figure 8d). This leads to the transition of orographically induced precipitation into Meiyu frontal precipitation between 08:00 LST and 12:00 LST. Under the P2 type, a persistent southwesterly geostrophic wind dominates the DM. The diurnal cycle of the southwesterly ageostrophic wind and its associated convergence resembles that of the P1 type. However, the northeasterly ageostrophic wind is positioned north of the DM region. Although it converges with the

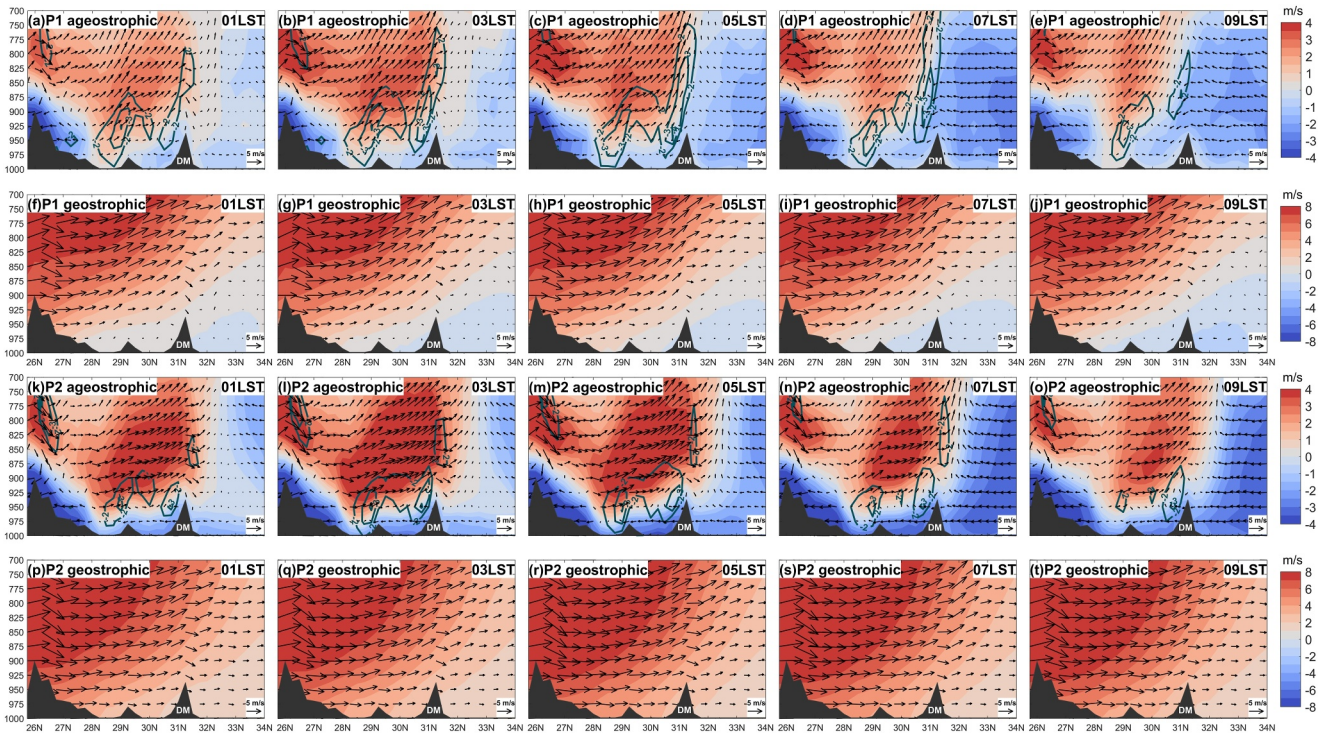

Figure 8. Diurnal variations in ageostrophic wind vectors (arrows), horizontal ageostrophic wind speed (shading), and divergence contributed by ageostrophic wind (contour in green solid lines, values shown by the numbers along the vertical profile, unit: 10-5/s) on extreme rainfall days under the P1 type projected onto the vertical cross-section (blue solid line in Figures 5b and 5c) every two hours starting from 01:00 LST are shown from (a to e). As in panels (f–j), but for geostrophic wind and divergence contributed by geostrophic wind. As in panels (k–o), but for ageostrophic wind and divergence contributed by ageostrophic wind on extreme rainfall days under the P2 type. As in panels (p–t), but for geostrophic wind and divergence contributed by geostrophic wind. The vertical wind has been reduced by half to show it more clearly. The black shading at the bottom of each picture indicates the terrain height (unit, m) along the vertical cross-section.

southwesterly ageostrophic wind, this convergence is weaker than in the P1 type and occurs farther north, contributing little to the extreme rainfall in the DM.

The diurnal cycles of low-level ageostrophic winds and their associated convergence are in good agreement with the diurnal cycles of extreme rainfall as shown in Figure 8. Since the strongest southwesterly ageostrophic winds occur at 875 hPa under both synoptic patterns, the following analysis focuses on this level. Under the P1 type, the ageostrophic wind over the southwestern side of the DM rotates clockwise to align with the southwesterly geostrophic wind, strengthening the southwesterly wind and creating the strongest convergence along the southwestern windward slope at 05:00 LST (Figure 9d). Over the northeastern side of the DM, the ageostrophic wind also rotates clockwise, peaking as a strong northeasterly wind at 07:00 LST (Figure 9e), and converges with the southwesterly ageostrophic wind within the DM region, as the front lies within this area. Under the P2 type, ageostrophic winds on either side of the front exhibit similar clockwise rotations. However, the DM is primarily affected by the ageostrophic wind south of the front since the front is located at the northern side outside the DM region.

The above analysis proves that the diurnal variation in low-level ageostrophic wind is the primary driver of the diurnal cycle of extreme rainfall in the DM. Under both synoptic patterns, the extreme rainfall center along the southwestern windward slope is related to the diurnal peak of the southwesterly ageotrophic wind southwest of the DM, which is blocked and lifted by the DM. The prolonged high extreme rainfall intensity under the P1 type can be attributed to the convergence of the southwesterly and northeasterly ageostophic winds. This difference is induced by the different circulations and their interactions with the terrain under varying synoptic patterns.

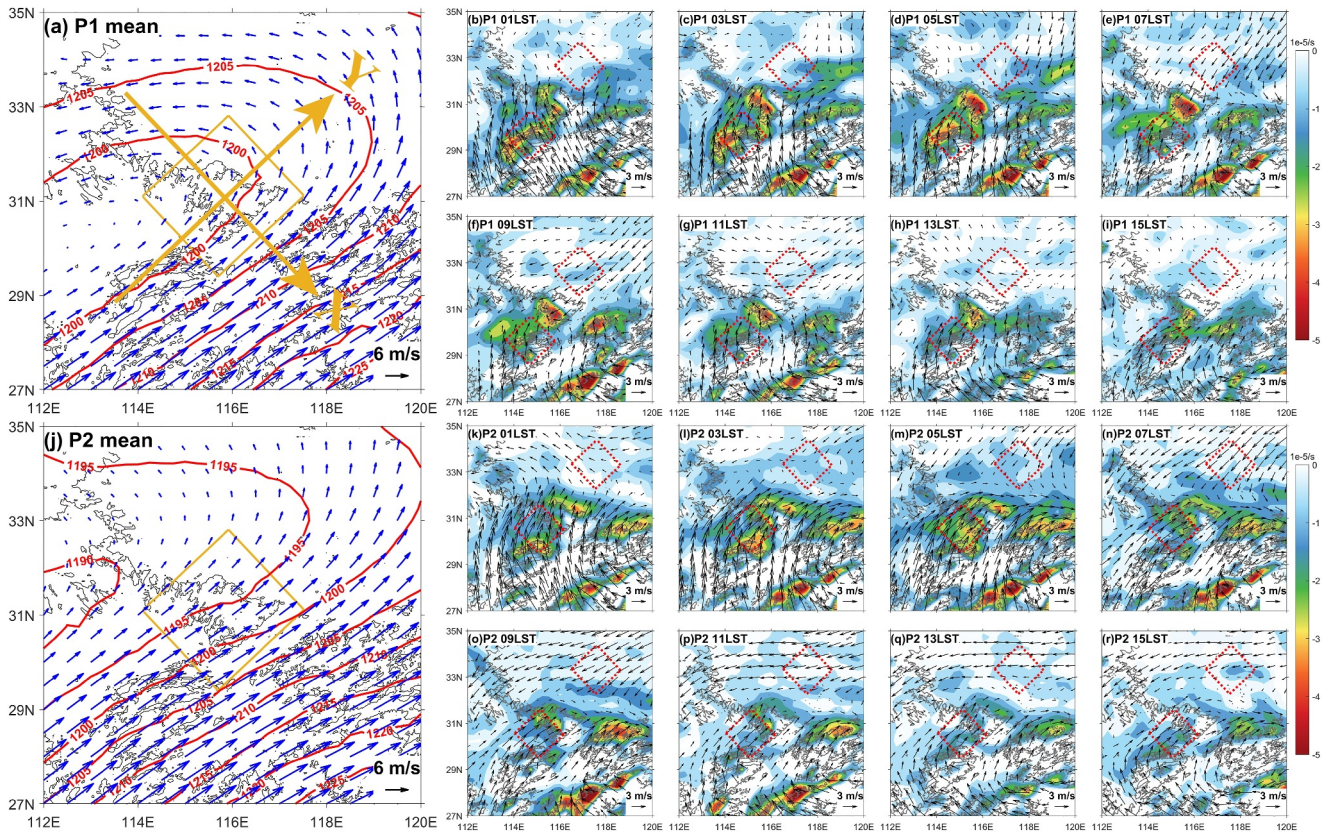

Figure 9. The composite daily mean geostrophic wind vectors (blue arrows) and geopotential height (red lines) at 875 hPa on extreme rainfall days under the P1 type (a) and the P2 type (j). Diurnal change of the composite ageostrophic wind vectors (arrows) and divergence caused by the ageostrophic wind (shading) at 875 hPa on extreme rainfall days of the P1 type from (b–i) every two hours starting from 01:00 LST. As in panels (k–r), but for the P2 type. The shallow gray lines denote the terrain height of 200 and 1,500 m. The yellow rectangle in panels (a, j) represents the DM region. The axis in panel (a) is the axis used for the horizontal momentum budget analysis in subsection 4.3. The red dashed line rectangles in panels (b–i) and (k–r) denote the area used in the horizontal momentum budget analysis.

4.3. Mechanisms of the Ageostrophic Wind

The previous subsection demonstrates that the diurnal variations in low-level ageostrophic winds can explain the diurnal cycles of extreme rainfall under the two synoptic patterns. However, the causes of these diurnal variations in ageostrophic winds require further clarification.

As shown in Figure 9, ageostrophic winds rotate clockwise around geostrophic winds. When they align, the low-level wind in the direction of the geostrophic wind reaches its daily peak. To identify the forces driving the morning low-level wind maximum due to the diurnal variation in ageostrophic wind, we analyze the time series of wind acceleration and the forces of the horizontal momentum budget along the *y*-axis in Figure 10. The daily mean southwesterly winds are approximately perpendicular to the southwestern windward slope of the DM and the daily mean geostrophic wind closely resembles the daily mean total wind. Consequently, the coordinate axes are rotated such that the new *y*-axis is aligned with the direction of the southwesterly winds, as illustrated in Figure 9. The terms in Equation 2 are averaged over the two dashed red rectangles in Figure 9, representing the horizontal momentum budget analysis for the southwestern and northeastern regions of the convergence area. The terms in the northeastern region have been sign-reversed to align with the direction of the northeasterly wind. The diurnal variation of the AD term is comparatively smaller than that of the other terms, so it is not analyzed.

Under both synoptic patterns, the horizontal momentum budget analysis shows similar characteristics. On the southwestern side of the DM, the southwesterly wind strengthens at night, with the CFA and TW terms showing consistent trend and sign. This indicates that the PGF and Coriolis force dominate the acceleration of the southwesterly wind. During the daytime, especially in the morning when the TW term peaks, the southwesterly wind weakens. At this time, the TW and FF terms share the same sign, and the variation in the TW term is

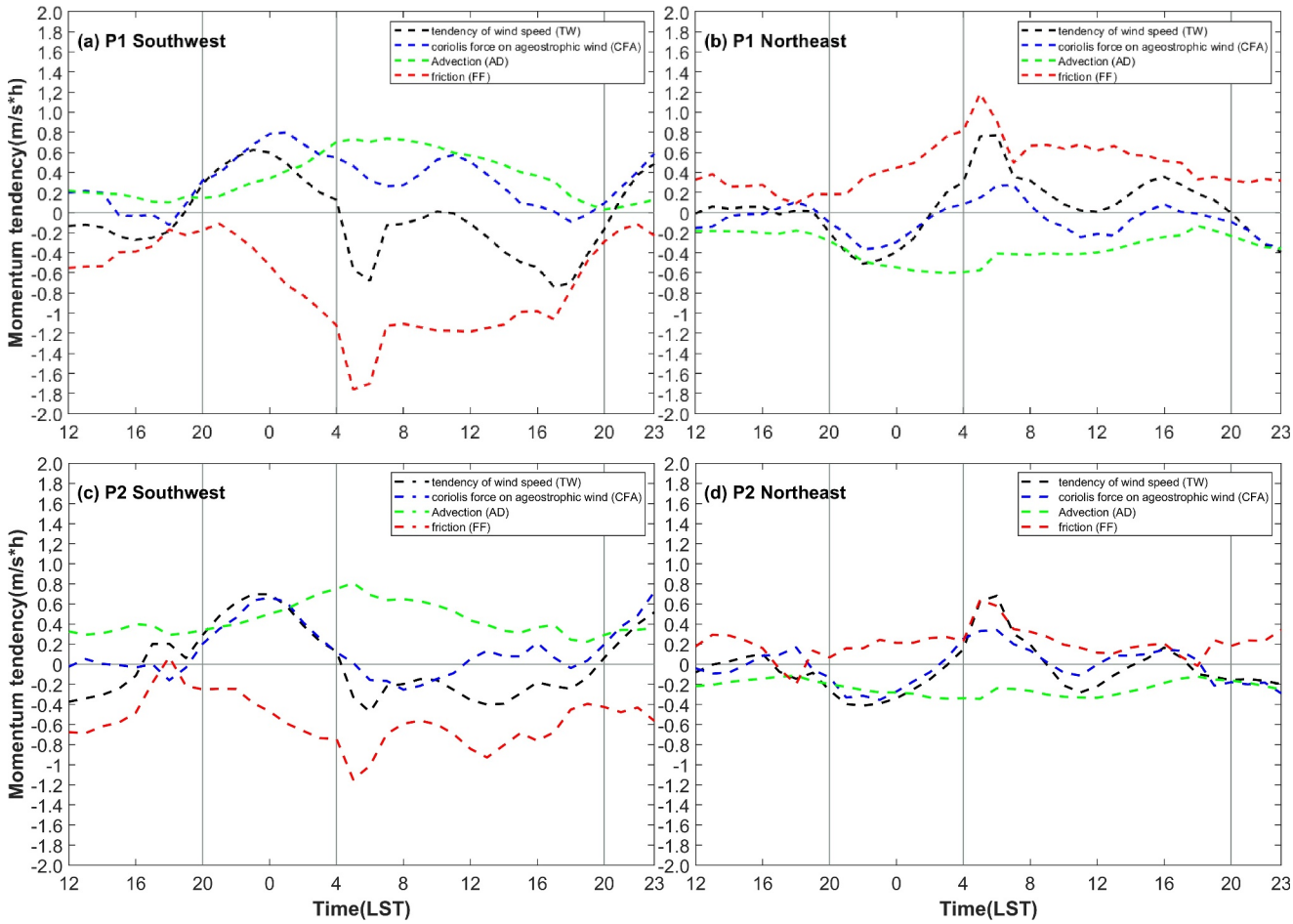

Figure 10. Variations of the TW term, the CFA term, the AD term, and the FF term in the horizontal momentum equation averaged over the southwestern and northeastern regions indicated by the dashed line red rectangles in Figure 9 at 875 hPa under the P1 type (a, b) during extreme rainfall days and the preceding 12 hours. As in panels (c, d), but for the P2 type.

significantly influenced by the FF term, suggesting that the FF governs the deceleration of the southwesterly wind. On the northeastern side of the DM, the deceleration of the southwesterly wind is accompanied by the acceleration of the northeasterly wind. During the daytime, the strengthening northeasterly wind converges with the southwesterly wind, enhancing the frontal zone in the morning. The mechanisms driving the diurnal variation of the northeasterly wind are similar to those of the southwesterly wind.

The results are consistent with Blackadar's theory of inertial oscillation, explaining the nighttime-to-morning acceleration of low-level winds on both sides of the front during extreme rainfall days under both synoptic patterns. During the daytime, a well-mixed boundary layer allows ground friction to influence the entire layer, maintaining a near balance among PGF, Coriolis force, and friction. At night, surface cooling increases static stability, suppressing deep vertical mixing. The upper boundary layer becomes free from friction, and the three-force balance breaks down. Therefore, winds deviate from the geostrophic balance state through inertial oscillation, leading to the occurrence of ageostrophic winds. The low-level winds become super-geostrophic and accelerate during nighttime (Blackadar, 1957; Du et al., 2015; Fu et al., 2019).

To further investigate the causes of the differences in ageostrophic winds during extreme rainfall days under the two synoptic patterns, we derived the diagnostic equations of ageostrophic winds by transforming the horizontal momentum equations, based on Xia et al. (2023). Figure 11 exhibits the diurnal variations in ageostrophic winds and their components after decomposition. During extreme rainfall days under both synoptic patterns, ageostrophic winds on the northern and southern sides of the front show clockwise diurnal variations and converge in the morning. Under the P1 type, convergence occurs within the DM region, while under the P2 type, it is located

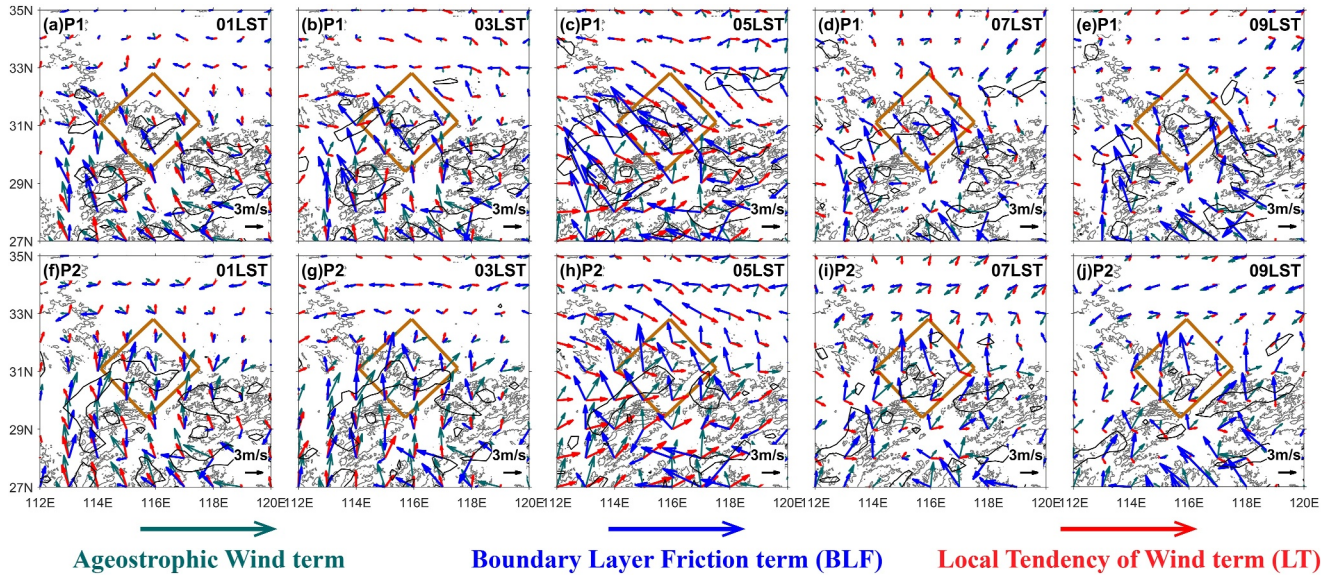

Figure 11. Horizontal distribution of the diurnal variation in ageostrophic winds at 875 hPa (green arrows) contributed by the LT term (red arrows) and the boundary layer friction (BLF) term (blue arrows) every two hours starting from 01:00 LST under the P1 type (a–e). As in panels (f–j), but for the P2 type. The black solid line indicates the divergence contour of 0.4 × 10-5/s contributed by the BLF term. The shallow gray lines denote the terrain height of 200 and 1,500 m.

north of the DM region. The diagnostic results show that ageostrophic winds are mainly driven by the LT and BLF terms, with other terms contributing minimally and not discussed further. The LT term dominates the diurnal clockwise rotations of ageostrophic winds, although its wind speed is smaller than that of the BLF term. While the diurnal variations of the BLF term are less pronounced, its wind speed is greater. Under both synoptic patterns, the BLF term primarily contributes to the convergence of ageostrophic winds from both sides of the front. However, the intensity and locations of convergence differ. Since the magnitude of the BLF term is proportional to the total wind speed and its direction generally points to the right of the horizontal wind, the differences in convergence are mainly driven by variations in large-scale circulations.

In summary, during extreme rainfall days under both synoptic patterns, the diurnal variations in the ageostrophic winds on both sides of the front are primarily driven by inertial oscillation. However, under the P1 type, the convergence region is located directly above the DM and is relatively stronger. Whereas under the P2 type, it is situated to the north of the DM and is weaker. These differences are primarily attributed to variations in large-scale circulations.

4.4. Diurnal Cycles of Low-Level Vortice

The above sections have demonstrated that the inertial oscillation of the low-level ageostrophic wind plays an important role in modulating the diurnal cycle of extreme rainfall. However, under both synoptic patterns, fronts are present during extreme rainfall days. In previous studies, MCVs have been found to exist along the Meiyu front. These MCVs contribute to the occurrence of extreme rainfall and exhibit certain diurnal variation characteristics (Zhang et al., 2018). Under both synoptic patterns, the Barnes band-pass filtered horizontal wind field and relative vorticity field at 875 hPa reveal a low-level vortice over the DM and surrounding areas. Thus, in this subsection, we will examine whether the low-level vortice has a distinct diurnal cycle related to the diurnal cycle of extreme rainfall.

At approximately 114°E, a low-level vortice forms at different latitudes during extreme rainfall days under both synoptic patterns (Figure 12). This vortice reaches a maximum horizontal extent of about 200 km at peak intensity, matching the spatial scale of the DM. Under the P1 type, the low-level vortice develops on the southwestern side of the DM region, strengthening from late morning to early afternoon, coinciding with the period of sustained extreme rainfall. Similarly, under the P2 type, the low-level vortice follows a comparable diurnal cycle but is located north of the DM region, exerting minimal influence on extreme rainfall in the DM. Li et al. (2022) demonstrated that the windward slope of the DM induces positive PV anomalies and then reinforces the local

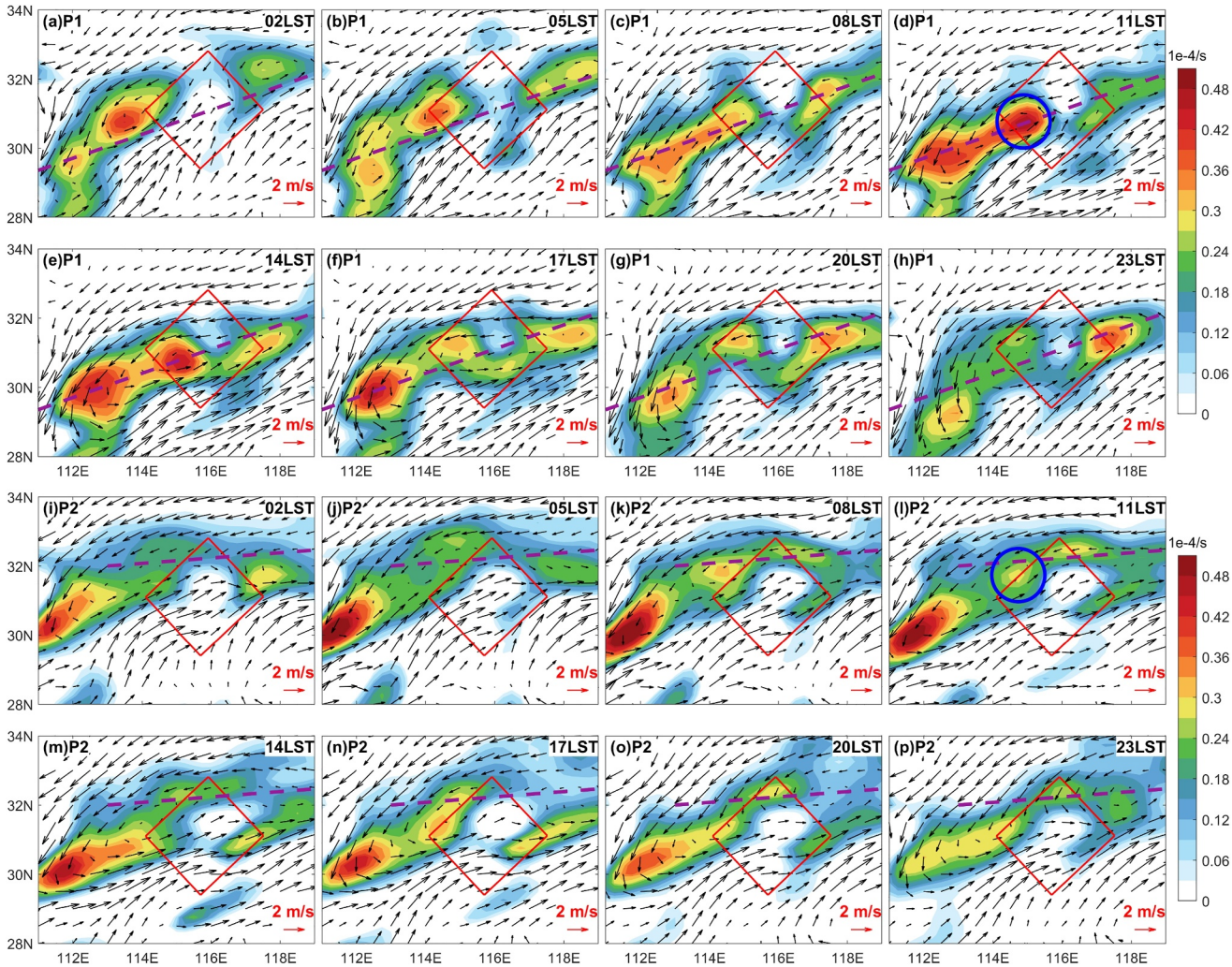

Figure 12. Diurnal change of the composite mesoscale relative vorticity (shading) and horizontal wind vectors after using a Barnes-band-pass filter at 850 hPa on extreme rainfall days under the P1 type from (a to h) every three hours starting from 02:00 LST. As in panels (i–p), but for the P2 type. The red rectangle represents the DM region. The purple dashed line is the front defined in Figure 6. The targeted low-level vortice is indicated by the blue circle.

precipitation through the orographic lifting and blocking effects. Therefore, the low-level vortice may interact with the terrain and contribute to the maintenance of the high extreme rainfall intensity under the P1 type. However, under the current assumptions, the mechanisms governing the formation and organization of this low-level vortice, as well as quantitative estimation of its contribution of this low-level vortice to extreme rainfall require further investigation.

5. Summary and Discussion

The DM, as a typical mesoscale terrain in the YHRB, serves as one of the primary precipitation centers during summer. In the present study, we use statistical methods to investigate the factors contributing to the summer extreme rainfall in the DM and its diurnal cycle under specific synoptic patterns. The main findings are as follows:

The occurrence and characteristics of the summer extreme rainfall in the DM are closely linked to specific synoptic patterns. Summer extreme rainfall is most likely to occur under the southwesterly monsoon conditions, accounting for 90% of the total extreme rainfall amount. Compared to the environments during rainfall days, the multi-scale weather systems associated with extreme rainfall are significantly stronger, featuring intensified low-level southwesterly winds, fronts, and low-level vortices. Their interactions with the terrain enhance moisture

transport and strengthen low-level convergence in the DM, collectively creating a more favorable environment for the development of extreme rainfall.

When extreme rainfall occurs under the P1 and P2 types, variations in the position of the Meiyu front lead to different large-scale circulations. However, the precipitation centers consistently form on the southwestern windward slope, highlighting the spatial locking effect of the DM on extreme rainfall.

Under the influence of different large-scale circulations, the diurnal cycles of extreme rainfall exhibit distinct characteristics closely linked to the inertial oscillation of low-level ageostrophic winds on the northern and southern sides of the front. The southwesterly ageostrophic winds south of the DM peak around 03:00 LST, contributing to the extreme rainfall peak at around 09:00 LST along the southwestern windward slope. Meanwhile, north of the DM, northeasterly ageostrophic winds peak around 07:00 LST and converge with the southwesterly ageostrophic winds. Due to differences in the relative positions of the front and the DM region, the convergence zone is located above the DM under the P1 type but shifts north of it under the P2 type. As a result, convergence sustains intense extreme rainfall under the P1 type but has relatively weaker impact under the P2 type.

Driven by the southwesterly monsoon, the diurnal variations in low-level ageostrophic winds result from the Blackadar inertial oscillation. However, their characteristics vary across different synoptic patterns, interacting with multi-scale weather systems and the DM to shape distinct diurnal cycles of extreme rainfall by regulating water vapor flux and upward motion. Since this study relies on statistical methods and reanalysis data with low vertical resolution and relatively poor lower-troposphere data quality, quantifying the contributions of uplift motions associated with low-level winds, low-level vortices, and terrain to extreme rainfall remains challenging. Additionally, the mechanisms governing the initiation and organization of low-level vortices cannot be fully understood through statistical analysis alone. In future research, we plan to conduct case studies of typical extreme rainfall using observational data and composite simulation methods (Chen et al., 2016) to explore the specific processes, detailed mechanisms, and quantitative contributions of various factors to extreme rainfall in the DM.

Conflict of Interest

The authors declare no conflicts of interest relevant to this study.

Data Availability Statement

The precipitation data used in the present study is the high spatiotemporal precipitation product provided by the National Meteorological Information Center of China (Chen et al., 2025; Shen et al., 2014). The ERA5 hourly reanalysis data on pressure levels is provided by ECMWF (Copernicus Climate Change Service (C3S), 2017; Hersbach et al., 2020). The open-source software cost733class version 1.2 is used to perform the PCT classification (Philipp et al., 2010). Now version 1.4 of this software is available (Philipp, 2013).

Acknowledgments
This work was primarily supported by the National Natural Science Foundation of China (Grants 42230607, 41875053, 61827901, and 42305006), the Open Grants of the State Key Laboratory of Severe Weather (Grant 2024LASW-A02), the Jianghuai Meteorological Joint Project of Anhui Natural Science Foundation (Grant 2408055UQ002), as well as the Tropical Cyclone Cloud Microphysical Observation Experiment. The authors are grateful to the National Meteorological Information Center of China for providing the high spatiotemporal precipitation product and the ECMWF for providing the ERA5 reanalysis data.

References

Barnes, S. L. (1973). *Mesoscale objective map analysis using weighted time-series observations* (p. 60). NOAA Tech. Memo. ERL NSSL-62, National Severe Storms Laboratory, Norman.

Blackadar, A. K. (1957). Boundary layer wind maxima and their significance for the growth of nocturnal inversions. *Bulletin of the American Meteorological Society*, *38*(5), 283–290. https://doi.org/10.1175/1520-0477-38.5.283

Carbone, R. E., Tuttle, J. D., Ahijevych, D. A., & Trier, S. B. (2002). Inferences of predictability associated with warm season precipitation episodes. *Journal of the Atmospheric Sciences*, *59*(13), 2033–2056. https://doi.org/10.1175/15200469(2002)059<2033:IOPAWW>2.0.CO;2

Cattell, R. B. (1966). The Scree test for the number of factors. *Multivariate Behavioral Research*, *1*(2), 245–276. https://doi.org/10.1207/s15327906mbr0102_10

Chen, C., Zhao, K., Huang, A., Zhou, A., Wang, C., Lu, Y., & Wang, S. (2025). The high spatiotemporal precipitation product over Dabie Mountain for the summers from 2008 to 2020 [Dataset]. *Zenodo*. https://doi.org/10.5281/zenodo.15844804

Chen, G., Sha, W., Iwasaki, T., & Ueno, K. (2012). Diurnal variation of rainfall in the Yangtze River Valley during the spring-summer transition from TRMM measurements. *Journal of Geophysical Research*, *117*(D6), D06106. https://doi.org/10.1029/2011JD017056

Chen, G., Sha, W., Iwasaki, T., & Wen, Z. (2017). Diurnal cycle of a heavy rainfall corridor over East Asia. *Monthly Weather Review*, *145*(8), 3365–3389. https://doi.org/10.1175/MWR-D-16-0423.1

Chen, G., Sha, W., Sawada, M., & Iwasaki, T. (2013). Influence of summer monsoon diurnal cycle on moisture transport and precipitation over eastern China. *Journal of Geophysical Research: Atmospheres*, *118*(8), 3163–3177. https://doi.org/10.1002/jgrd.50337

Chen, T., Chen, Y., Zheng, L., Chen, S., Chen, B., & Xu, J. (2024). The relationship between diurnal variations of precipitation and boundary layer winds over the Dabie Mountains during May–July. *Acta Meteorologica Sinica*, *82*(5), 615–631. https://doi.org/10.11676/qxxb2024.20230108

Chen, X., Zhang, F., & Zhao, K. (2016). Diurnal variations of the land–sea breeze and its related precipitation over South China. *Journal of the Atmospheric Sciences*, *73*(12), 4793–4815. https://doi.org/10.1175/JAS-D-160106.1

Chen, X., Zhao, K., & Xue, M. (2014). Spatial and temporal characteristics of warm season convection over Pearl River Delta region, China, based on 3 years of operational radar data. *Journal of Geophysical Research: Atmospheres*, *119*(22), 12–447. https://doi.org/10.1002/2014JD021965

Chen, Z. M. (1994). A simple technique of separation of mesoscale form from meteorological data (in Chinese). *Meteorological Monthly*, *20*(7), 39–42. https://doi.org/10.1002/2014JD021965

Clark, R. T., Wu, P., Zhang, L., & Li, C. (2021). The anomalous Mei-Yu rainfall of summer 2020 from a circulation clustering perspective: Current and possible future prevalence. *Advances in Atmospheric Sciences*, *38*(12), 2010–2022. https://doi.org/10.1007/s00376-021-1086-y

Copernicus Climate Change Service (C3S). (2017). ERA5: Fifth generation of ECMWF atmospheric reanalyses of the global climate [Dataset]. *Copernicus Climate Change Service Climate Data Store (CDS), date of access*. Retrieved from https://cds.climate.copernicus.eu/cdsapp

Cui, C., Zhou, W., Yang, H., Wang, X., Deng, Y., Wang, X., et al. (2023). Analysis of the characteristics of the low level jets in the middle reaches of the Yangtze River during the Mei-Yu season. *Advances in Atmospheric Sciences*, *40*(4), 711–724. https://doi.org/10.1007/s00376-022-2107-1

Dai, A. (2001). Global precipitation and thunderstorm frequencies. Part II: Diurnal variations. *Journal of Climate*, *14*(6), 1112–1128. https://doi.org/10.1175/1520-0442(2001)014<1112:GPATFP>2.0.CO;2

Ding, Y. (1992). Summer monsoon rainfalls in China. *Journal of the Meteorological Society of Japan. Ser. II*, *70*(1B), 373–396. https://doi.org/10.2151/jmsj1965.70.1B_373

Ding, Y. H. (1993). *Study on the lasting heavy rainfalls over the Yangtze-Huaihe River Basin in 1991(in Chinese) [M]* (p. 255). Beijing: Chinese Meteorological Press.

Du, Y., Rotunno, R., & Zhang, Q. (2015). Analysis of WRF-Simulated diurnal boundary layer winds in eastern China using a simple 1D model. *Journal of the Atmospheric Sciences*, *72*(2), 714–727. https://doi.org/10.1175/JAS-D-14-0186.1

Du, Y., Zhang, Q., Ying, Y., & Yang, Y. (2012). Characteristics of low-level jets in Shanghai during the 2008–2009 warm seasons as inferred from wind profiler radar data. *Journal of the Meteorological Society of Japan, Ser. II*, *90*(6), 891–903. https://doi.org/10.2151/jmsj.2012-603

Fang, Z. (1985). The preliminary study of medium-scale cloud clusters over the Changjiang basin in summer. *Advances in Atmospheric Sciences*, *2*(3), 334–340. https://doi.org/10.1007/BF02677249

Fu, P., Zhu, K., Zhao, K., Zhou, B., & Xue, M. (2019). Role of the nocturnal low-level jet in the formation of the morning precipitation peak over the Dabie Mountains. *Advances in Atmospheric Sciences*, *36*(1), 15–28. https://doi.org/10.1007/s00376-018-8095-5

Fu, S. M., Sun, J. H., Luo, Y. L., & Zhang, Y. C. (2017). Formation of long-lived summertime mesoscale vortices over central east China: Semi-idealized simulations based on a 14-year vortex statistic. *Journal of the Atmospheric Sciences*, *74*(12), 3955–3979. https://doi.org/10.1175/JAS-D-16-0328.1

He, H., & Zhang, F. (2010). Diurnal variations of warm-season precipitation over northern China. *Monthly Weather Review*, *138*(4), 1017–1025. https://doi.org/10.1175/2010MWR3356.1

He, Z., Zhang, Q., Bai, L., & Meng, Z. (2017). Characteristics of mesoscale convective systems in central East China and their reliance on atmospheric circulation patterns. *International Journal of Climatology*, *37*(7), 3276–3290. https://doi.org/10.1002/joc.4917

Hersbach, H., Bell, B., Berrisford, P., Hirahara, S., Horányi, A., Muñoz-Sabater, J., et al. (2020). The ERA5 global reanalysis. *Quarterly Journal of the Royal Meteorological Society*, *146*(730), 1999–2049. https://doi.org/10.1002/qj.3803

Houze Jr, R. A. (2012). Orographic effects on precipitating clouds. *Reviews of Geophysics*, *50*(1), RG1001. https://doi.org/10.1029/2011RG000365

Huth, R. (1993). An example of using obliquely rotated principal components to detect circulation types over Europe. Meteorologische Zeitschrift. *Neue Folge; (Germany)*, *2*(6), 285–293. https://doi.org/10.1127/metz/2/1993/285

Huth, R. (1996). An intercomparison of computer assisted circulation classification methods. *International Journal of Climatology*, *16*(8), 893–922. https://doi.org/10.1002/(SICI)10970088(199608)16:8<893::AID-JOC51>3.0.CO;2-Q

Huth, R. (1996b). Properties of the circulation classification scheme based on the rotated principal component analysis. *Meteorology and Atmospheric Physics*, *59*(3–4), 217–233. https://doi.org/10.1007/BF01030145

Huth, R. (2000). A circulation classification scheme applicable in GCM studies. *Theoretical and Applied Climatology*, *67*(1–2), 1–18. https://doi.org/10.1007/s007040070012

Jones, P. D., Horton, E. B., Folland, C. K., Hulme, M., Parker, D. E., & Basnett, T. A. (1999). The use of indices to identify changes in climatic extremes. *Climatic Change*, *42*(1), 131–149. https://doi.org/10.1023/A:1005468316392

Joyce, R. J., Janowiak, J. E., Arkin, P. A., & Xie, P. (2004). CMORPH: A method that produces global precipitation estimates from passive microwave and infrared data at high spatial and temporal resolution. *Journal of Hydrometeorology*, *5*(3), 487–503. https://doi.org/10.1175/1525-7541(2004)005<0487:CAMTPG>2.0.CO;2

Li, C., Li, Y., Fu, S., Jiang, X., Wang, X., Li, S., et al. (2022). A new perspective on the orographic effect of the windward slope on the multi-scale eastward-moving southwest vortex systems. *Atmospheric Research*, *279*, 106365. https://doi.org/10.1016/j.atmosres.2022.106365

Luo, Y., & Du, Y. (2023). The roles of low-level jets in "21·7" Henan extremely persistent heavy rainfall event. *Advances in Atmospheric Sciences*, *40*(3), 350–373. https://doi.org/10.1007/s00376-022-2026-1

Ni, T., Huang, Y., Ling, X. F., et al. (2018). Analysis of the characteristics of precipitation in the Dabie Mountains[J] (in Chinese). *Meteorological Science and Technology*, *46*(3), 556–562. https://doi.org/10.19517/j.1671-6345.20170280

Ninomiya, K. (2000). Large-and meso-α-scale characteristics of Meiyu/Baiu front associated with intense rainfalls in 1–10 July 1991. *Journal of the Meteorological Society of Japan. Ser. II*, *78*(2), 141–157. https://doi.org/10.2151/jmsj1965.78.2_141

O'Lenic, E. A., & Livezey, R. E. (1988). Practical considerations in the use of Rotated Principal Component Analysis (RPCA) in diagnostic studies of upper-air height fields. *Monthly Weather Review*, *116*(8), 1682–1689. https://doi.org/10.1175/15200493(1988)116<1682:PCITUO>2.0.CO;2

Philipp, A. (2009). Comparison of principal component and cluster analysis for classifying circulation pattern sequences for the European domain. *Theoretical and Applied Climatology*, *96*(1–2), 31–41. https://doi.org/10.1007/s00704-008-0037-1

Philipp, A. (2013). Cost733class (version 1.4) [Software]. https://git.rz.uni-augsburg.de/philipan/cost733class-1.4

Philipp, A., Bartholy, J., Beck, C., Erpicum, M., Esteban, P., Fettweis, X., et al. (2010). Cost733cat-A database of weather and circulation type classifications. *Physics and Chemistry of the Earth, Parts A/B/C*, *35*(9–12), 360–373. https://doi.org/10.1016/j.pce.2009.12.010

Philipp, A., Beck, C., Huth, R., & Jacobeit, J. (2016). Development and comparison of circulation type classifications using the COST 733 dataset and software. *International Journal of Climatology*, *36*(7), 2673–2691. https://doi.org/10.1002/joc.3920

Rao, X., Zhao, K., Chen, X., Huang, A., Xue, M., Zhang, Q., & Wang, M. (2019). Influence of synoptic pattern and low-level wind speed on intensity and diurnal variations of orographic convection in summer over Pearl River Delta, South China. *Journal of Geophysical Research: Atmospheres*, *124*(12), 6157–6179. https://doi.org/10.1029/2019JD030384

Shen, Y., Zhao, P., Pan, Y., & Yu, J. (2014). A high spatiotemporal gauge-satellite merged precipitation analysis over China. *Journal of Geophysical Research: Atmospheres*, *119*(6), 3063–3075. https://doi.org/10.1002/2013JD020686

Shuqing, S., & Ming, Y. (1999). Subtropical high anomalies over the Western Pacific and its relations to the Asian monsoon and SST anomaly. *Advances in Atmospheric Sciences*, *16*(4), 559–568. https://doi.org/10.1007/s00376-999-0031-2

Sun, J., & Zhang, F. (2012). Impacts of mountain–plains solenoid on diurnal variations of rainfalls along the Mei-Yu front over the east China plains. *Monthly Weather Review*, *140*(2), 379–397. https://doi.org/10.1175/MWR-D-11-00041.1

Sun, J. H., Zhang, X. L., Qi, L. L., Zhang, G. Y., Zhao, S. X., & Tao, S. Y. (2004). An analysis on MCSs in Meiyu front during 20–24 June 2002. *Acta Meteorologica Sinica*, *62*(4), 423–438. https://doi.org/10.11676/qxxb2004.043

Tao, S. Y. (1987). A review of recent research on the East Asian summer monsoon in China. *Monsoon meteorology*, 60–92. https://doi.org/10.2151/jmsj.87.381

Tu, K., Yan, Z., & Dong, W. (2010). Climatic jumps in precipitation and extremes in drying North China during 1954-2006. *Journal of the Meteorological Society of Japan. Ser. II*, *88*(1), 29–42. https://doi.org/10.2151/jmsj.2010-103

Wallace, J. M. (1975). Diurnal variations in precipitation and thunderstorm frequency over the conterminous United States. *Monthly Weather Review*, *103*(5), 406–419. https://doi.org/10.1175/1520-0493(1975)103<0406:DVIPAT>2.0.CO;2

Wang, C., Zhao, K., Huang, A., Chen, X., & Rao, X. (2021). The crucial role of synoptic pattern in determining the spatial distribution and diurnal cycle of heavy rainfall over the South China Coast. *Journal of Climate*, *34*(7), 2441–2458. https://doi.org/10.1175/JCLI-D-20-0274.1

Wang, Q., & Tan, Z. (2009). Idealized numerical simulation study of the potential vorticity banners over a mesoscale Mountain: Dry adiabatic process. *Advances in Atmospheric Sciences*, *26*(5), 906–922. https://doi.org/10.1007/s00376-009-8004-z

Wang, Q., Xue, M., & Tan, Z. (2016). Convective initiation by topographically induced convergence forcing over the Dabie Mountains on 24 June 2010. *Advances in Atmospheric Sciences*, *33*(10), 1120–1136. https://doi.org/10.1007/s00376-016-6024-z

Wang, Q. W., & Tan, Z. M. (2006). Flow regimes for major topographic obstacles of China. *Chinese Journal of Geophysics*, *49*(4), 866–877. https://doi.org/10.1002/cjg2.906

Wu, Z. X., Luo, Y. L., Liu, X., & Cheng, D. B. (2022). Statistical characteristics of the hourly heavy rainfall events over Anhui province during the 2011-2018 warm seasons and the associated synoptic circulation patterns [J] (in Chinese). *Meteorological Monthly*, *48*(8), 963–978. https://doi.org/10.7519/j.issn.1000-0526.2022.041001

Xia, F., Huang, X., Fei, J., Wang, J., Cheng, X., & Zhang, C. (2023). Mechanisms of ageostrophic wind convergence in the boundary layer of coastal warm-sector extreme heavy rainfall in south China. *Journal of Geophysical Research: Atmospheres*, *128*(19), e2022JD038472. https://doi.org/10.1029/2022JD038472

Xu, J., Zhang, Q., Bi, B., & Chen, Y. (2022). Spring extreme precipitation days in north China and their reliance on atmospheric circulation patterns during 1979–2019. *Journal of Climate*, *35*(7), 2253–2267. https://doi.org/10.1175/JCLI-D-21-0268.1

Xu, W., & Zipser, E. J. (2011). Diurnal variations of precipitation, deep convection, and lightning over and east of the eastern Tibetan Plateau. *Journal of Climate*, *24*(2), 448–465. https://doi.org/10.1175/2010JCLI3719.1

Xu, X., Huang, A., Huang, D., Zhang, Y., Gu, C., Cai, S., et al. (2023). What are the dominant synoptic patterns leading to the summer regional hourly extreme precipitation events over central-eastern Tibetan Plateau and Sichuan Basin? *Geophysical Research Letters*, *50*(5), e2022GL102342. https://doi.org/10.1029/2022GL102342

Xu, X., Xue, M., Wang, Y., & Huang, H. (2017). Mechanisms of secondary convection within a Mei-Yu frontal mesoscale convective system in eastern China. *Journal of Geophysical Research: Atmospheres*, *122*(1), 47–64. https://doi.org/10.1002/2016JD026017

Xu, Y. T., & Ding, Y. H. (1988). Objective analysis of meteorological fields and meso-scale filtering (in Chinese). *Chinese Journal of Atmospheric Sciences*, *12*(3), 274–282. https://doi.org/10.1016/0011-7471(76)90822-6

Xue, M., Luo, X., Zhu, K., Sun, Z., & Fei, J. (2018). The controlling role of boundary layer inertial oscillations in Meiyu frontal precipitation and its diurnal cycles over China. *Journal of Geophysical Research: Atmospheres*, *123*(10), 5090–5115. https://doi.org/10.1029/2018JD028368

Yan, Y., & Coauthors. (2019). Synoptic patterns and sounding derived parameters associated with summertime heavy rain fall in Beijing. *International Journal of Climatology*, *39*, 1476–1489. https://doi.org/10.1002/joc.5895

Yang, G. Y., & Slingo, J. (2001). *The diurnal cycle in the tropics* (Vol. 129(4), pp. 784–801). Monthly Weather Review. https://doi.org/10.1175/15200493(2001)129<0784:TDCITT>2.0.CO;2

Yu, R., Li, J., Chen, H., & Yuan, W. (2014). Progress in studies of the precipitation diurnal variation over contiguous China. *Journal of Meteorological Research*, *28*(5), 877–902. https://doi.org/10.1029/2018JD028368

Yuan, W., Yu, R., Zhang, M., Lin, W., Chen, H., & Li, J. (2012). Regimes of diurnal variation of summer rainfall over subtropical East Asia. *Journal of Climate*, *25*(9), 3307–3320. https://doi.org/10.1175/JCLI-D-11-00288.1

Zeng, J., Huang, A., Wu, P., Huang, D., Zhang, Y., Tang, J., et al. (2023). Typical synoptic patterns responsible for summer regional hourly extreme precipitation events over the middle and lower Yangtze River basin, China. *Geophysical Research Letters*, *50*(17), e2023GL104829. https://doi.org/10.1029/2023GL104829

Zhang, A. Q., Chen, Y. L., Zhou, S. N., Cui, C. G., Wan, R., & Fu, Y. F. (2020). Diurnal variation of Meiyu rainfall in the Yangtze Plain during atypical Meiyu years. *Journal of Geophysical Research: Atmospheres*, *125*(1), e2019JD031742. https://doi.org/10.1029/2019JD031742

Zhang, C., Huang, X., Fei, J., Luo, X., & Zhou, Y. (2021). Spatiotemporal characteristics and associated synoptic patterns of extremely persistent heavy rainfall in southern China. *Journal of Geophysical Research: Atmosphere*, *126*(1), e2022JD036604. https://doi.org/10.1029/2020JD033253

Zhang, F. H., Chen, T., Zhang, F., Shen, X. L., & Lan, Y. (2020). Extreme features of severe precipitation in Meiyu period over the middle and lower reaches of Yangtze River basin in June–July 2020 (in Chinese). *Meteorological Monthly*, *46*(11), 1405–1414. https://doi.org/10.7519/j.issn.1000-0526.2020.11.002

Zhang, J. P., Fu, S. M., Sun, J. H., Shen, X. Y., & Zhang, Y. C. (2015). A statistical and compositional study on the two types of mesoscale vortices over the Yangtze River basin (in Chinese). *Climatic and Environmental Research*, *20*(3), 319–336. https://doi.org/10.3878/j.issn.1006-9585.2015.14164

Zhang, W. Y., & Wang, Q. W. (2021). Weather background types for the extreme precipitation occurred over the Dabie Mountain region (in Chinese). *Journal of the Meteorological Sciences*, *41*(2), 441–451. https://doi.org/10.12306/2020jms.000

Zhang, Y., Sun, J., & Fu, S. (2014). Impacts of diurnal variation of mountain-plain solenoid circulations on precipitation and vortices east of the Tibetan Plateau during the Mei-Yu season. *Advances in Atmospheric Sciences*, *31*(1), 139–153. https://doi.org/10.1007/s00376-013-2052-0

Zhang, Y., Zhang, F., Davis, C. A., & Sun, J. (2018). Diurnal evolution and structure of long lived mesoscale convective vortices along the Mei-Yu front over the East China plains. *Journal of the Atmospheric Sciences*, *75*(3), 1005–1025. https://doi.org/10.1175/JAS-D-17-0197.1

Zheng, L., Sun, J., Qiu, X., & Yang, Z. (2020). Five-year climatology of local convections in the Dabie Mountains. *Atmosphere*, *11*(11), 1246. https://doi.org/10.3390/atmos11111246

Zheng, Y., Xue, M., Li, B., Chen, J., & Tao, Z. (2016). Spatial characteristics of extreme rainfall over China with hourly through 24-hour accumulation periods based on national-level hourly rain gauge data. *Advances in Atmospheric Sciences*, *33*(11), 1218–1232. https://doi.org/10.1007/s00376-016-6128-5